

Video-Mirai: Autoregressive Video Diffusion Models Need Foresight

Yonghao Yu¹ Lang Huang^{2*} Runyi Li³ Zerun Wang¹ Toshihiko Yamasaki¹

¹The University of Tokyo ²National Institute of Informatics ³Peking University

{y_yu, ze_wang, yamasaki}@cvm.t.u-tokyo.ac.jp, lang@nii.ac.jp, lirunyi@stu.pku.edu.cn

Abstract

Causal video generators must predict from the past, but they need not learn only from it. In streaming autoregressive video diffusion, each emitted segment becomes a commitment that future segments must preserve. Standard training, however, only asks each causal state to explain the present. This creates what we call a representation-level planning gap: states that fit the current segment may discard identity, layout, and motion information needed for a consistent future. We introduce Video-Mirai, a training-only method that closes this gap without changing causal inference: the generator rolls out causally, a frozen foresight encoder reads the completed rollout non-causally, and a lightweight predictor distills the resulting stopped-gradient targets into causal states. Future frames supervise representations, never generator inputs. At inference, the encoder and predictor are discarded, leaving the original architecture, per-step FLOPs, and KV-cache behavior unchanged. Video-Mirai improves a strong Causal-Forcing baseline on 5-second VBench from 83.8 to 84.6 in terms of Total Score. On 30-second rollouts beyond the training horizon, subject consistency improves from 84.9 to 88.5 and background consistency from 90.2 to 91.9. Ablations identify future-conditioned targets as the key ingredient, and probes show that future frames become more decodable from current features. Causality should constrain inference, not representation supervision. Our study highlights that visual autoregressive models need foresight. Project Page: <https://yOuroy.github.io/Video-Mirai>.

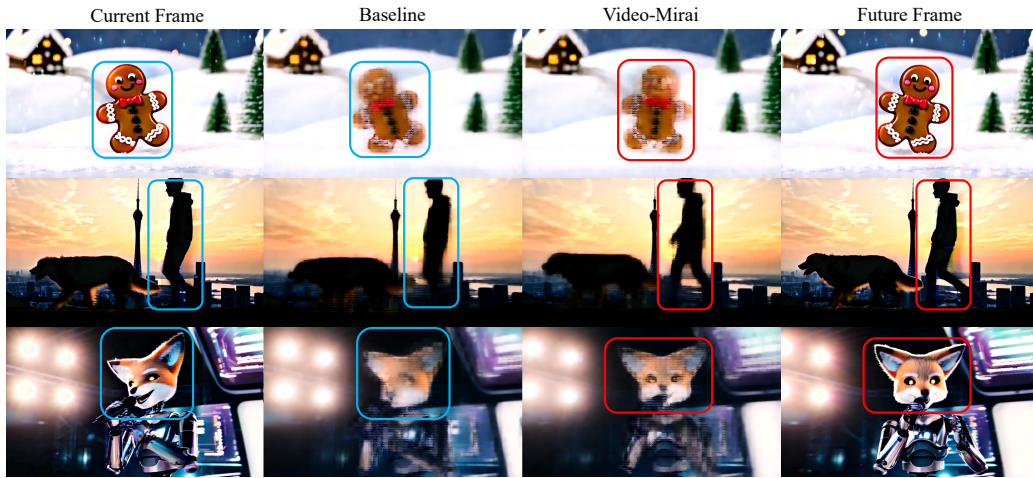


Figure 1: **Video-Mirai makes the future more decodable.** An MLP readout reconstructs future RGB from the frozen causal generator’s current hidden state. Left to right: current frame, baseline readout, Video-Mirai readout (ours), future frame. **blue/red**: regions matching the **current/future**.

*Corresponding author.



Figure 2: **Qualitative evidence of the planning gap.** Frames at $t=0s$, $2.5s$, $5s$ from the same prompt. The baseline’s local plausibility per segment abruptly drift between segments: the bear’s motion resets, and the woman’s identity and background change. Video-Mirai mitigates these breaks.

1 Introduction

Streaming video generation has a hidden burden: every emitted segment becomes a promise that future segments must keep. Autoregressive (AR) video diffusion follows this interface directly: generate a frame or chunk from the previous context, emit it, and continue. This streaming ability is central to low-latency visual synthesis for interactive world modeling [6, 1], game-engine simulation [32], and embodied intelligence [7, 31, 8]. Yet, it also makes local decisions hard to revise. A segment may look correct in isolation while failing to specify what must remain true later. Figure 2 shows typical failures: in the baseline rollouts, a bear’s motion unexpectedly jumps between frames; in another example, the people and the background abruptly change between segments. These errors suggest that local visual quality is not sufficient for maintaining identity, layout, and motion over time.

We view this as more than generic error accumulation. Present-segment supervision is under-constrained: many hidden states can generate the same plausible current segment, but only some retain the information needed for future consistency. The loss tells the model whether the *present* looks right given the *past*; it does not directly ask whether the current state contains the information *future* segments will need. We call this missing constraint a representation-level *planning gap*.

This gap points to a simple design principle: use foresight as supervision, not as input. Future evidence is useful for deciding which current states are good, but it cannot be given to a streaming generator at inference. We introduce Video-Mirai, a training-only objective for AR video diffusion that resolves this tension. During training, Video-Mirai lets future segments supervise the current causal state; at inference, the generator remains strictly past-only. Existing AR video methods improve how models roll out, but they do not close this planning gap. Self-Forcing [16] exposes the model to self-generated histories; Causal-Forcng [41] makes distillation compatible with causal decoding. These methods modify the history distribution and the output target. Video-Mirai targets a different object: the representation carried by the current causal state.

Video-Mirai is deliberately minimal. The generator first rolls out video causally under the same mask used at inference. A frozen foresight encoder then reads the completed rollout and produces future-informed feature targets for the current states. A lightweight predictor maps each causal hidden state to its corresponding foresight target with a cosine loss. Future segments are used only to construct stopped-gradient supervision; they are never provided as generator inputs. After training, the foresight encoder and predictor are discarded. The deployed generator remains exactly causal, with identical architecture, attention pattern, per-step FLOPs, and KV-cache behavior to the baseline.

Video-Mirai improves both short- and long-horizon generation. On the 5-second VBench, Video-Mirai improves the AR video diffusion baseline Causal-Forcng from 83.82 to 84.62 in Total Score. For the 30-second generation, beyond the training horizon, subject consistency improves from 84.93 to 88.47, and background consistency from 90.22 to 91.94. The method also transfers across AR settings, improving both frame-wise and chunk-wise generation. Beyond generation metrics, representation

probes (Figures 1 and 5) show that future frames become substantially more decodable from frozen Video-Mirai features. Figure 2 confirms that this internalized foresight translates to visibly more coherent rollouts, mitigating the planning gap in practice. Unlike prior foresight objectives for image autoregression, Video-Mirai addresses a video-specific planning gap in causal diffusion rollouts, where future supervision must improve temporal coherence while preserving streaming inference and KV-cache-compatible deployment. In summary, our contributions are threefold:

- We formulate foresight prediction as a representation-level objective for causal video generation, using future-aware targets during training while preserving strictly causal inference.
- Video-Mirai improves AR video generation across frame-wise and chunk-wise settings, with gains that also extend to 30-second rollouts beyond the training horizon.
- We identify which foresight source, prediction layer, predictor design, and look-ahead window make the training signal effective, and verify through probes that future content becomes more decodable from frozen features.

2 Related Work

2.1 Video Diffusion Models

Large-scale video diffusion models such as Wan [33], CogVideoX [35], HunyuanVideo [20], and MovieGen [27] generate high-fidelity clips by jointly denoising a temporal window, allowing bidirectional interactions among frames within the clip. This full-window interface supports strong short-range consistency, but it is less natural for low-latency settings where frames or chunks should be emitted as soon as they are generated. AR video diffusion instead generates frames or chunks sequentially from past context, enabling streaming inference and supporting rollouts beyond the training horizon, albeit with increasing risk of drift. CausVid [38], Diffusion-Forcing [7], MAGI-1 [31], and SkyReels-V2 [8] exemplify this causal direction. A complementary line extends pretrained video diffusion models at test time through streaming or queue-based protocols without retraining, including StreamingT2V [13] and FIFO-Diffusion [19]. Together, these works expose the tradeoff behind our study: streaming generation requires local causal decisions, while coherent video depends on identity, layout, and motion remaining predictable over future segments.

2.2 Distillation and Training Techniques for AR Video Diffusion

To deliver high-quality sampling in a few steps, recent work has focused on distilling bidirectional teachers [15, 30, 28, 23] into causal students via Distribution Matching Distillation (DMD) [37, 36], progressively closing several supervision gaps inherent to this process. Self-Forcing [16] closes the exposure-bias gap by performing AR rollout during training, exposing the student to its own imperfect histories under a holistic video-level loss. Causal-Forcing [41] identifies a theoretical flaw in ODE distillation initialization: distilling a bidirectional teacher into a causal student violates frame-level injectivity, thereby preventing the student from faithfully recovering the teacher’s flow map. They close this injectivity gap by introducing an AR teacher for ODE initialization. Rolling-Forcing [24] targets error accumulation over long horizons through joint denoising across a rolling window, attention-sink anchors, and training over extended non-overlapping windows. These methods advance the state of the art in causal training stability and past consistency. Our work is orthogonal to theirs. We address the complementary planning gap, namely, a causal generator’s inability to anticipate its own future evolution, and our foresight objective can be layered on top of these AR video diffusion training paradigms, as our experiments demonstrate.

2.3 Representation Alignment and Foresight

Aligning a model’s intermediate representations with those of a strong external encoder, dating back to knowledge distillation [14] and intermediate-layer hints [29], has proven more effective for training efficiency and sample quality than pixel-level objectives. REPA [39] regresses mid-layer DiT features onto a pretrained self-supervised encoder such as DINOv2 [25], with follow-ups [22] extending this to end-to-end VAE tuning. A separate line uses representation prediction as a self-supervised pretext task: V-JEPA and its successors [5, 2], building on JEPA [21, 3] and masked image modeling [12], predict masked spatiotemporal regions, with the action-conditioned V-JEPA-2-AC training a predictor

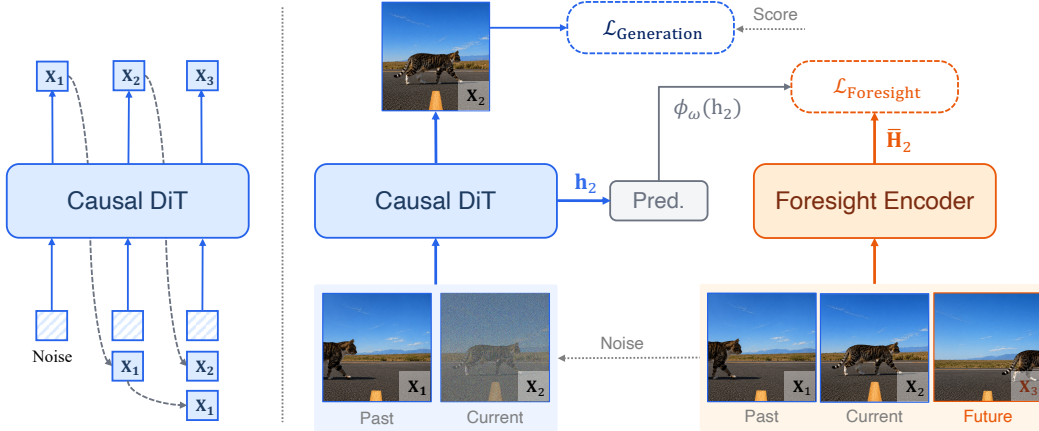


Figure 3: **Overview of Video-Mirai.** We take a three-segment video as an example. The causal DiT denoises \mathbf{X}_2 from its noisy version conditioned on \mathbf{X}_1 via KV-cache. A frozen foresight encoder processes the causal DiT’s clean rollout $\{\mathbf{X}_1, \mathbf{X}_2, \mathbf{X}_3\}$, including the future segment \mathbf{X}_3 . A predictor maps the causal DiT’s hidden state \mathbf{h}_2 into the encoder’s space, where the foresight loss aligns it with the encoder’s fused hidden state $\bar{\mathbf{H}}_2$, which contains foresight information.

invoked at inference. The intuition that future-aware signals improve training extends beyond vision, e.g., multi-token prediction [10] in language models.

Closest in spirit, Mirai [40] exposes AR *image* generators to future-position information. Video-Mirai extends this to causal *video diffusion*, where the planning gap is sharper: temporal coherence over multi-second rollouts is more demanding than spatial coherence within an image, and the bidirectional/causal architectural asymmetry inherent to video distillation has no counterpart in the image setting. Video-Mirai draws on REPA-style predictor alignment and JEPA-style latent prediction, recombined for a different purpose: future-aware supervision for a strictly causal video model. Unlike REPA, our target is the temporally shifted hidden state from a bidirectional video model. Unlike V-JEPA, our target is the encoder’s representation of the model’s own future rollout rather than masked regions, and our predictor is discarded after training. The causal model remains strictly causal at inference. To our knowledge, Video-Mirai is the first to use future-conditioned representation alignment as a training-only signal for causal video diffusion.

3 Method

3.1 Preliminaries

We consider AR video diffusion that distills a pretrained bidirectional diffusion model into a few-step causal generator G_θ . A video is a sequence of temporal segments $\mathbf{x} = \{\mathbf{X}_1, \dots, \mathbf{X}_N\}$, where a segment is a single latent frame (frame-wise) or a chunk of consecutive latent frames (chunk-wise). The causal constraint requires:

$$p_\theta(\mathbf{x}) = \prod_{i=1}^N p_\theta(\mathbf{X}_i | \mathbf{X}_{<i}), \quad (1)$$

so segment \mathbf{X}_i is generated from $\mathbf{X}_{<i}$ alone, with no access to $\mathbf{X}_{>i}$ at inference. Standard distillation pipelines such as Causal-Forcing [41] realize this through three stages: AR teacher fine-tuning, causal ODE distillation, and asymmetric DMD [37, 36]. We adopt this pipeline as our base.

The factorization in Eq. 1 only constrains each \mathbf{X}_i to be plausible given $\mathbf{X}_{<i}$. It says nothing about whether the hidden state \mathbf{h}_i^L used to generate \mathbf{X}_i retains the information needed to generate *future* segments coherently. Concretely, existing training objectives reduce to a present-segment loss:

$$\mathcal{L}_{\text{present}}(\theta) = \mathbb{E}_{\mathbf{x}} \sum_{i=1}^N \ell(G_\theta(\mathbf{X}_i | \mathbf{X}_{<i})), \quad (2)$$

where ℓ is any per-segment supervision applied to the model’s output distribution (DMD score, flow-matching, etc.). All such losses share one property: they only score what the generator *emits* for segment i , never the hidden state \mathbf{h}_i^L that produced it. Many distinct hidden states \mathbf{h}_i^L can

Table 1: **Foresight window comparison.** Effect of the offset set Δ on top of Causal-Forcing.

Setting	Δ	Quality \uparrow	Semantic \uparrow	Total \uparrow
Causal-Forcing	–	84.54	80.93	83.82
Current only	$\{0\}$	85.07	81.55	84.36
1-segment ahead only	$\{1\}$	84.82	81.50	84.15
Current + 1-segment ahead	$\{0, 1\}$	85.38	81.59	84.62
Current + 2-segment ahead	$\{0, 1, 2\}$	85.11	82.00	84.49

Table 2: **Projector architecture comparison.** Fusion means encoder targets are averaged across Δ before the loss; per-offset means each offset is handled separately.

Architecture	Target handling	Depth	Quality \uparrow	Semantic \uparrow	Total \uparrow
Causal-Forcing	–	–	84.54	80.93	83.82
MLP	Fusion	3	85.09	81.58	84.38
Multi-MLP	Per-offset	3	85.00	81.12	84.22
DiT	Fusion	2	85.14	81.85	84.48
DiT	Fusion	3	85.38	81.59	84.62
DiT	Fusion	4	85.41	81.19	84.57
DiT-AdaLN	Per-offset	3	85.34	81.46	84.56

drive the same \mathbf{X}_i to optimum: some retain identity, layout, and motion cues that future segments will need; others discard them. The loss has no preference between the two. We call this missing constraint the *representation-level planning gap*: the present-segment loss never asks whether \mathbf{h}_i^L is a good state from which to continue. Recent advances in AR video diffusion address adjacent yet distinct gaps, including exposure bias [16], ODE-distillation injectivity [41], and long-horizon error accumulation [24]. None of them, however, modifies what Eq. 2 asks of \mathbf{h}_i^L . They reshape the history distribution, the distillation initialization, or the rollout protocol, not the supervision applied to the causal state itself. The planning gap is therefore orthogonal to all three. Closing it requires supervising \mathbf{h}_i^L with a *foresight* signal: a target derived from the model’s own future rollout.

3.2 Video-Mirai

Figure 3 illustrates an overview of Video-Mirai: while denoising the current segment, the causal DiT generator’s mid-depth feature is fed to a predictor ϕ_ω to predict the foresight encoder’s feature on a future segment of the same rollout, via a cosine similarity loss:

$$\ell_i^{\bar{F}}(\delta) = 1 - \cos(\phi_\omega(\mathbf{h}_i^L), \text{sg}[\mathbf{H}_{i+\delta}^{L'}]). \quad (3)$$

Let $\mathbf{h}_i^L \in \mathbb{R}^{T \times d_c}$ denote the causal generator’s hidden state at layer L when generating \mathbf{X}_i , and $\mathbf{H}_{i+\delta}^{L'} \in \mathbb{R}^{T \times d_f}$ the foresight encoder’s hidden state on the causal generator’s rollout segment $\mathbf{X}_{i+\delta}$ at a matched mid-depth layer L' , computed when the encoder processes the full rollout \mathbf{x} . Two design questions follow immediately: (i) is foresight useful, and how far ahead should the alignment look, and (ii) should multiple offsets be combined by fusing targets or by averaging losses. We answer both before assembling the full objective.

Foresight window. We compare four offset configurations: current only ($\{0\}$), one-segment ahead only ($\{1\}$), current plus one-segment ($\{0, 1\}$), and current plus two-segment ($\{0, 1, 2\}$). In the chunk-wise setting, $\delta=1$ corresponds to a 3-latent-frame look-ahead. As shown in Table 1, current plus one-segment ($\{0, 1\}$) yields the best Quality and Total Scores. Crucially, even current-only alignment carries foresight information because the foresight encoder here is bidirectional, so its hidden state on the current chunk is already conditioned on future chunks. Thus, foresight arises not only from explicit future-offset alignment but also from implicit future information through bidirectional attention. Extending the window to $\{0, 1, 2\}$ further improves Semantic but degrades Quality, indicating that longer-range alignment trades visual fidelity for global coherence.

Target fusion vs. per-offset losses. Given a window $\Delta = \{0, 1, \dots, K\}$ ($K=1$ by default), we can either compute one loss per offset and average, or fuse the encoder’s features across Δ into a single target and align once. Table 2 compares four projector designs spanning these two regimes: the pointwise MLP and the DiT projector, each on either the fused target or a per-offset variant. Two

Table 3: **Injection depth comparison.** Each row pairs a causal generator layer with a foresight encoder layer at matched relative depth α .

Layers (α)	Quality \uparrow	Semantic \uparrow	Total \uparrow
Causal-Forcing	84.54	80.93	83.82
9 \rightarrow 12 (0.3)	85.14	81.37	84.39
15 \rightarrow 20 (0.5)	85.38	81.59	84.62
24 \rightarrow 32 (0.8)	84.77	81.54	84.12

Table 4: **Foresight encoder comparison.** All variants use the default 3-block DiT projector, layered on Causal-Forcing chunk-wise.

Encoder	Quality \uparrow	Semantic \uparrow	Total \uparrow
Causal-Forcing	84.54	80.93	83.82
EMA	84.36	81.95	83.88
Wan-1.3B	84.41	82.19	83.96
Wan-14B	85.38	81.59	84.62

findings emerge. First, fusing targets consistently outperforms averaging losses. The single-head MLP beats Multi-MLP, and the single-head DiT beats DiT-AdaLN. Fusing across offsets gives the causal generator an averaged future representation rather than any specific sample, stabilizing optimization and matching our finding (§4.3) that Video-Mirai’s features encode a *distribution* over futures rather than a single committed continuation. Second, DiT outperforms the pointwise MLP at matched depth, suggesting the alignment benefits from token mixing. We also vary DiT depth among $\{2, 3, 4\}$ blocks and find that 3 blocks give the best Total Score. We therefore adopt a 3-block DiT with target fusion as our default. With this choice, the fused target and per-segment loss are:

$$\bar{\mathbf{H}}_i = \frac{1}{|\Delta|} \sum_{\delta \in \Delta} \mathbf{H}_{i+\delta}^{L'}, \quad \ell_i^F = 1 - \cos(\phi_\omega(\mathbf{h}_i^L), \text{sg}[\bar{\mathbf{H}}_i]). \quad (4)$$

Training. At each step, the causal generator unrolls a video \mathbf{x} segment by segment from noise, following the standard few-step denoising loop of Causal-Forcing with the usual KV-cache, and we cache its mid-depth states $\{\mathbf{h}_i^L\}$. The frozen foresight encoder then processes the full rollout \mathbf{x} in a single forward pass at zero diffusion timestep, yielding $\{\mathbf{H}_i^{L'}\}$. For every segment with a near-future target available ($i \leq N - K$), $\phi_\omega(\mathbf{h}_i^L)$ is pulled toward the fused target $\bar{\mathbf{H}}_i$ via Eq. 4, combined with the asymmetric DMD generation loss:

$$\mathcal{L}_{\text{total}} = \mathcal{L}_{\text{Generation}} + \lambda \underbrace{\frac{1}{N - K} \sum_{i=1}^{N-K} \ell_i^F}_{\mathcal{L}_{\text{Foresight}}}, \quad (5)$$

where we use $\lambda = 0.2$ by default. The DMD term scores a re-noised version of the same rollout against a frozen Wan-14B real-score teacher and a Wan-1.3B fake-score critic, following Self-Forcing [16]. The remaining designs, such as the foresight encoder, injection depth L , and loss form, are ablated in §4.2. We also discuss applying Video-Mirai in a different stage in Appendix D.4.

4 Experimental Results

4.1 Setup

Implementation details. We use Wan2.1-T2V-1.3B [33] (henceforth Wan-1.3B) as the causal generator backbone, which generates 81-frame videos at a resolution of 832×480 . Our main results are reported on top of the three-stage Causal-Forcing [41] pipeline under the chunk-wise setting, where each segment is a chunk of 3 consecutive latent frames. The training procedure in every stage follows Causal-Forcing. We also use Video-Mirai as a drop-in addition to Self-Forcing [16] and to the frame-wise Causal-Forcing variant. Unless otherwise noted, Video-Mirai uses Wan2.1-T2V-14B (henceforth Wan-14B) as the foresight encoder. All distillation runs use $8 \times$ H100 GPUs with gradient accumulation 8. The training prompts come from the filtered VidProM [34] extension released by Self-Forcing. Other training settings follow the baseline’s recipe. More details are in Appendix A.

Evaluation. We evaluate on VBench [17]. For 5-second generation, each score is the mean over 5 generated videos per prompt across the full VBench prompt set, following the benchmark’s standard protocol. For the 30-second long-horizon evaluation, we roll out the same trained checkpoints on 200 randomly selected MovieGen [27] prompts, following the Rolling-Forcing [24] protocol, and report the subset of VBench dimensions that are computable under its prompt-agnostic protocol. Due to the high cost of video distillation, we follow prior work and report paired prompt-level bootstrap significance instead of variance over multiple training seeds. Details are provided in Appendix E.

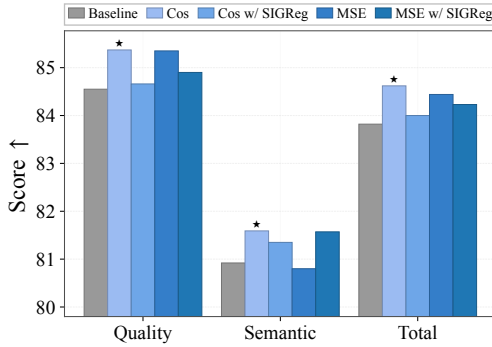


Figure 4: **Foresight loss comparison.** Cosine similarity vs. MSE, with and without the SIGReg. layers and horizons.

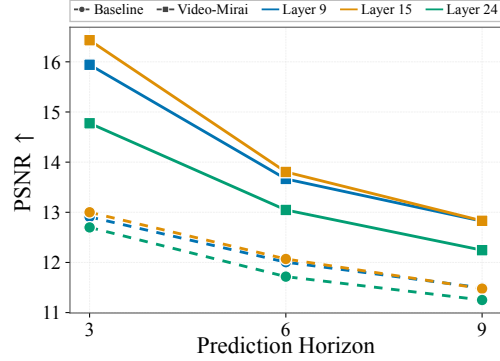


Figure 5: **Future-frame readout fidelity across layers and horizons.**

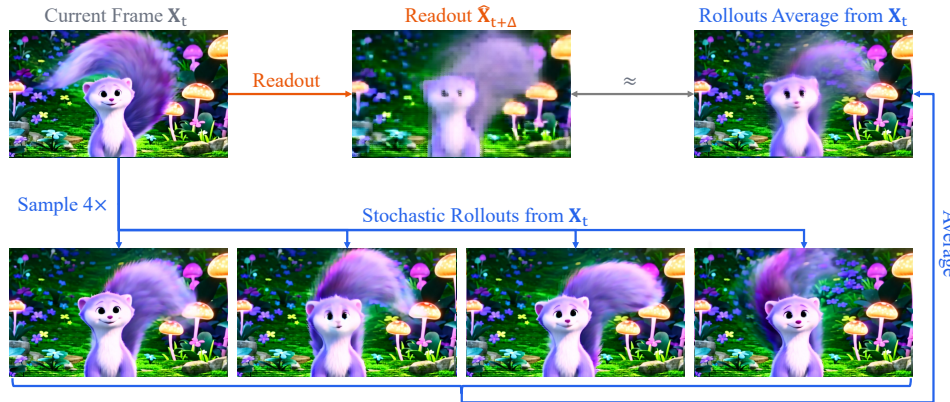


Figure 6: **Video-Mirai internalizes the future distribution.** The readout matches the rollout average.

4.2 Component-wise analysis

Injection depth. Foresight injection requires choosing both a causal generator layer L and an encoder layer L' . Since the causal generator (30 blocks) and the encoder (40 blocks) differ in depth, we pair layers at matched relative depth: $L = \alpha D_s$, $L' = \alpha D_t$. Table 3 shows that mid-depth ($\alpha=0.5$) is best. Shallow layers have not yet accumulated the abstract planning features that benefit from foresight, while deep layers are close to pixel-level reconstruction and have less freedom to be reshaped by an auxiliary objective. We adopt $\alpha=0.5$ throughout.

Foresight encoder. We compare three foresight encoders that span two axes, causality and capacity: the EMA copy of the causal generator itself, the bidirectional Wan-1.3B and Wan-14B models. The results in Table 4 show that Wan-14B dominates Quality and Total Score, while Wan-1.3B achieves the highest Semantic Score. Among the smaller encoders, Wan-1.3B’s bidirectional attention provides larger gains than the causal EMA. We adopt Wan-14B as our default, since it is already the real-score model in the baseline DMD pipeline, without adding any parameters at deployment.

Foresight loss. Figure 4 compares different foresight losses with or without a signal-regularization term (SIGReg) [4]. Cosine similarity alone works best. We attribute this to two effects. First, MSE forces the generator’s feature to match the encoder’s direction, scale, and full coordinate distribution, pulling it away from its native feature geometry and dropping the Semantic Score. Second, adding SIGReg consistently degrades the Total Score under both losses, indicating that explicitly shaping the projected feature distribution toward isotropic Gaussianity conflicts with the alignment objective. We adopt cosine similarity without SIGReg as the default. Loss weight ablations are in Appendix D.3.

4.3 Foresight Visualization

All evidence so far is behavioral: VBench scores improve after foresight training. A sharper question is whether foresight is actually *internalized* into the causal generator’s representations. We design a representational probing experiment to answer this directly.

Table 5: **Quantitative comparisons with existing methods.** On 5-second VBench, Video-Mirai achieves the best Quality, Semantic, and Total Scores while preserving the throughput and latency of the underlying AR baseline.

Model	#Params	Resolution	Throughput (FPS) \uparrow	Latency (s) \downarrow	Quality Score \uparrow	Semantic Score \uparrow	Total Score \uparrow
<i>Bidirectional Video Diffusion Models</i>							
LTX-Video [11]	1.9B	768 \times 512	8.98	13.5	81.88	71.62	79.83
Wan2.1 [33]	1.3B	832 \times 480	0.78	103	84.30	79.65	83.37
<i>Autoregressive Video Diffusion Models</i>							
NOVA [9]	0.6B	768 \times 480	0.88	4.1	80.66	78.92	80.31
Pyramid Flow [18]	2B	640 \times 384	6.70	2.5	83.41	70.11	80.75
SkyReels-V2 [8]	1.3B	960 \times 540	0.49	112	83.96	74.01	81.97
MAGI-1 [31]	4.5B	832 \times 480	0.19	282	81.67	67.72	78.88
<i>Distilled Autoregressive Video Models</i>							
CausVid [38]	1.3B	832 \times 480	17.0	0.69	83.98	70.72	81.33
Self-Forcing [16] (chunk-wise)	1.3B	832 \times 480	17.0	0.69	84.37	80.87	83.67
+ Video-Mirai (Ours)	1.3B	832 \times 480	17.0	0.69	84.82	81.45	84.15
Causal-Forcing [41] (frame-wise)	1.3B	832 \times 480	8.9	0.45	83.16	78.73	82.27
+ Video-Mirai (Ours)	1.3B	832 \times 480	8.9	0.45	84.59	79.66	83.60
Causal-Forcing [41] (chunk-wise)	1.3B	832 \times 480	17.0	0.69	84.54	80.93	83.82
+ Video-Mirai (Ours)	1.3B	832 \times 480	17.0	0.69	85.38	81.59	84.62

Table 6: **System-level comparison on VBench.** Left: 5-second generation. Right: 30-second long-horizon generation. Video-Mirai is applied as a drop-in addition on top of Self-Forcing and Causal-Forcing under both chunk-wise and frame-wise generation.

Method	5-second			30-second		
	Subject Consistency \uparrow	Background Consistency \uparrow	Overall Consistency \uparrow	Subject Consistency \uparrow	Background Consistency \uparrow	Overall Consistency \uparrow
Self-Forcing (chunk-wise)	96.18	96.43	26.70	89.83	92.72	25.02
+ Video-Mirai (Ours)	96.77	96.85	26.84	91.62	93.77	25.33
Causal-Forcing (frame-wise)	90.67	92.97	26.42	75.60	84.41	23.25
+ Video-Mirai (Ours)	93.13	94.12	26.57	76.90	85.07	23.66
Causal-Forcing (chunk-wise)	96.05	95.92	26.83	84.93	90.22	24.93
+ Video-Mirai (Ours)	96.41	96.54	26.85	88.47	91.94	25.03

Probe setup. We take two frozen causal generators with identical architectures: the Causal-Forcing baseline and Video-Mirai. For each model, we train a small MLP decoder to reconstruct the clean RGB future frame δ chunks ahead from the model’s layer-15 hidden state on the *current* chunk. No foresight predictor is used at probing time; the decoder is purely a readout. Decoders for the two models are trained separately within an identical budget. If Video-Mirai has internalized future information, its features should support substantially more faithful future reconstructions.

Qualitative and quantitative readout. Figure 1 shows three probe samples. We can see that Video-Mirai faithfully reconstructs the future frame, while the baseline stays anchored to the current, as expected for a feature that lacks foresight. We then quantify the readout fidelity at scale across three feature-extraction layers $L \in \{9, 15, 24\}$ and three prediction horizons of $\{3, 6, 9\}$ frames ahead, which means chunk $\delta \in \{1, 2, 3\}$, reporting MSE, PSNR, and LPIPS. For each layer, we train a separate MLP decoder on the causal generator’s hidden state and evaluate on held-out prompts. For brevity, we plot PSNR in Figure 5. The MSE and LPIPS curves, which show the same trend, are provided in Appendix F. Video-Mirai consistently outperforms the baseline at every layer and every horizon across all three metrics. The gap is largest at near horizons, where foresight supervision applies most directly, and persists at $\delta=9$ frames, well beyond the training-time foresight window, indicating that foresight internalization generalizes rather than memorizes.

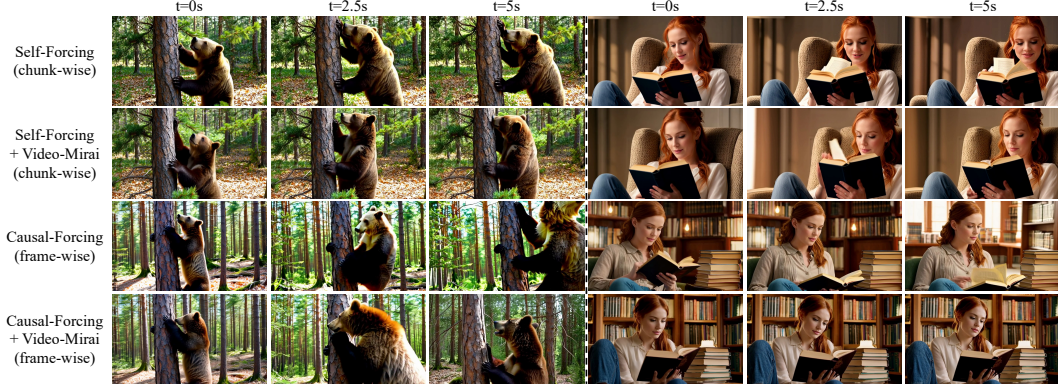


Figure 7: **Qualitative comparison.** Representative frames at $t=0s$, $2.5s$, $5s$ from the rollouts of the same prompt under the baselines and their Video-Mirai counterparts. Video-Mirai rollouts preserve subject identity and scene composition more reliably across time.

Distribution of futures. The probes above show that Video-Mirai’s features support future readout, but the future of a given current is not deterministic. Running the causal generator from the same current with different noise seeds yields a distribution of valid futures. So do the features encode a specific future, or the *distribution* of futures? Figure 6 visualizes this. We sample four independent rollouts from the same current under different noise seeds, confirming that the future is genuinely stochastic. For example, the purple ermine’s tail ends up at different positions across rollouts. The readout from Video-Mirai’s current segment closely matches the *average* of these four rollouts. The readout can already capture identity, layout, and motion statistics of the future before any of those future frames are actually generated. Video-Mirai’s mid-depth features encode a probabilistic summary of what is about to happen, not a single sampled continuation.

4.4 System-Level Comparison

Table 5 situates Video-Mirai within the broader landscape of video diffusion models, comparing against bidirectional, AR, and distilled-AR video diffusion models on VBench. We apply Video-Mirai as a drop-in addition on top of three distilled-AR baselines: Self-Forcing chunk-wise and Causal-Forcing in both frame-wise and chunk-wise variants. The results show that Video-Mirai improves Quality, Semantic, and Total Scores at every baseline, confirming that foresight internalization transfers across backbones and across frame-wise and chunk-wise generation. Figures 2 and 7 show representative qualitative comparisons. Additional examples are in Appendix G.

The improvement extends to 30-second long-horizon generation, on precisely the dimensions tied to causal short-sightedness: subject consistency, background consistency, and overall consistency all improve substantially over the no-foresight baseline as shown in Table 6. In chunk-wise settings, the 30-second gains are substantially larger than the 5-second gains across all three consistency dimensions, confirming that the planning gap widens with rollout length and is exactly where foresight pays off. This performance is achieved at identical inference cost, since the foresight encoder and predictor are discarded after training. Training-time overhead is analyzed in Appendix B.

5 Conclusion

We introduced Video-Mirai, a training-only paradigm that closes the representation-level planning gap in causal AR video diffusion: a single cosine alignment loss pulls the causal generator’s mid-depth features toward a frozen bidirectional encoder’s view of its own rollout. At inference, the encoder and predictor are discarded, leaving the architecture, per-step FLOPs, and KV-cache behavior unchanged. As a drop-in addition to AR video models, Video-Mirai lifts Causal-Forcing’s VBench scores at 5 seconds and widens the margin at 30-second generation. Representation probes confirm that future information is internalized into the causal weights, turning anticipation into a property of the causal forward pass. Limitations are discussed in Appendix C. Our results argue that causality is a constraint on inference, not on what training can teach a model to anticipate.

References

- [1] Eloi Alonso, Adam Jelley, Vincent Micheli, Anssi Kanervisto, Amos Storkey, Tim Pearce, and François Fleuret. Diffusion for world modeling: Visual details matter in atari. In *NeurIPS*, volume 37, pages 58757–58791, 2024.
- [2] Mahmoud Assran, Adrien Bardes, David Fan, Quentin Garrido, et al. V-jepa 2: Self-supervised video models enable understanding, prediction and planning. *arXiv preprint arXiv:2506.09985*, 2025.
- [3] Mahmoud Assran, Quentin Duval, Ishan Misra, Piotr Bojanowski, Pascal Vincent, Michael Rabbat, Yann LeCun, and Nicolas Ballas. Self-supervised learning from images with a joint-embedding predictive architecture. In *CVPR*, pages 15619–15629, 2023.
- [4] Randall Balestriero and Yann LeCun. LeJEPa: Provable and scalable self-supervised learning without the heuristics. *arXiv preprint arXiv:2511.08544*, 2025.
- [5] Adrien Bardes, Quentin Garrido, Jean Ponce, Xinlei Chen, Michael Rabbat, Yann LeCun, Mahmoud Assran, and Nicolas Ballas. Revisiting feature prediction for learning visual representations from video. *TMLR*, 2024.
- [6] Jake Bruce, Michael D. Dennis, Ashley Edwards, Jack Parker-Holder, Yuge Shi, Edward Hughes, Matthew Lai, Aditi Mavalankar, Richie Steigerwald, Chris Apps, et al. Genie: Generative interactive environments. In *ICML*, pages 4603–4623, 2024.
- [7] Boyuan Chen, Diego Marti Monso, Yilun Du, Max Simchowitz, Russ Tedrake, and Vincent Sitzmann. Diffusion forcing: Next-token prediction meets full-sequence diffusion. In *NeurIPS*, volume 37, pages 24081–24125, 2024.
- [8] Guibin Chen, Dixuan Lin, Jiangping Yang, Chunze Lin, Junchen Zhu, Mingyuan Fan, Hao Zhang, Sheng Chen, Zheng Chen, Chengcheng Ma, et al. SkyReels-V2: Infinite-length film generative model. *arXiv preprint arXiv:2504.13074*, 2025.
- [9] Haoge Deng, Ting Pan, Haiwen Diao, Zhengxiong Luo, Yufeng Cui, Huchuan Lu, Shiguang Shan, Yonggang Qi, and Xinlong Wang. Autoregressive video generation without vector quantization. In *ICLR*, 2025.
- [10] Fabian Gloeckle, Badr Youbi Idrissi, Baptiste Rozière, David Lopez-Paz, and Gabriel Synnaeve. Better & faster large language models via multi-token prediction. In *ICML*, pages 15706–15734, 2024.
- [11] Yoav HaCohen, Nisan Chiprut, Benny Brazowski, Daniel Shalem, Dudu Moshe, Eitan Richardson, Eran Levin, Guy Shiran, Nir Zabari, Ori Gordon, Poriya Panet, Sapir Weissbuch, Victor Kulikov, Yaki Bitterman, Zeev Melumian, and Ofir Bibi. LTX-Video: Realtime video latent diffusion. *arXiv preprint arXiv:2501.00103*, 2024.
- [12] Kaiming He, Xinlei Chen, Saining Xie, Yanghao Li, Piotr Dollár, and Ross Girshick. Masked autoencoders are scalable vision learners. In *CVPR*, pages 15979–15988, 2022.
- [13] Roberto Henschel, Levon Khachatryan, Hayk Poghosyan, Daniil Hayrapetyan, Vahram Tadevosyan, Zhangyang Wang, Shant Navasardyan, and Humphrey Shi. StreamingT2V: Consistent, dynamic, and extendable long video generation from text. In *CVPR*, pages 2568–2577, 2025.
- [14] Geoffrey Hinton, Oriol Vinyals, and Jeff Dean. Distilling the knowledge in a neural network. *arXiv preprint arXiv:1503.02531*, 2015.
- [15] Jonathan Ho, Ajay Jain, and Pieter Abbeel. Denoising diffusion probabilistic models. In *NeurIPS*, volume 33, pages 6840–6851, 2020.
- [16] Xun Huang, Zhengqi Li, Guande He, Mingyuan Zhou, and Eli Shechtman. Self forcing: Bridging the train-test gap in autoregressive video diffusion. In *NeurIPS*, 2025.

- [17] Ziqi Huang, Yinan He, Jiashuo Yu, Fan Zhang, Chenyang Si, Yuming Jiang, Yuanhan Zhang, Tianxing Wu, Qingyang Jin, Nattapol Chanpaisit, Yaohui Wang, Xinyuan Chen, Limin Wang, Dahua Lin, Yu Qiao, and Ziwei Liu. VBench: Comprehensive benchmark suite for video generative models. In *CVPR*, pages 21807–21818, 2024.
- [18] Yang Jin, Zhicheng Sun, Ningyuan Li, Kun Xu, Kun Xu, Hao Jiang, Nan Zhuang, Quzhe Huang, Yang Song, Yadong Mu, and Zhouchen Lin. Pyramidal flow matching for efficient video generative modeling. In *ICLR*, 2025.
- [19] Jihwan Kim, Junoh Kang, Jinyoung Choi, and Bohyung Han. FIFO-Diffusion: Generating infinite videos from text without training. In *NeurIPS*, volume 37, pages 89834–89868, 2024.
- [20] Weijie Kong, Qi Tian, Zijian Zhang, Rox Min, Zuozhuo Dai, Jin Zhou, Jiangfeng Xiong, Xin Li, Bo Wu, Jianwei Zhang, et al. Hunyuanvideo: A systematic framework for large video generative models. *arXiv preprint arXiv:2412.03603*, 2024.
- [21] Yann LeCun. A path towards autonomous machine intelligence. *OpenReview preprint*, 2022. Version 0.9.2.
- [22] Xingjian Leng, Jaskirat Singh, Yunzhong Hou, Zhenchang Xing, Saining Xie, and Liang Zheng. Repa-e: Unlocking vae for end-to-end tuning with latent diffusion transformers. In *ICCV*, pages 18262–18272, 2025.
- [23] Yaron Lipman, Ricky T. Q. Chen, Heli Ben-Hamu, Maximilian Nickel, and Matt Le. Flow matching for generative modeling. In *ICLR*, 2023.
- [24] Kunhao Liu, Wenbo Hu, Jiale Xu, Ying Shan, and Shijian Lu. Rolling forcing: Autoregressive long video diffusion in real time. In *ICLR*, 2026.
- [25] Maxime Oquab, Timothée Darcet, Théo Moutakanni, Huy V. Vo, Marc Szafraniec, Vasil Khalidov, Pierre Fernandez, Daniel Haziza, Francisco Massa, Alaaeldin El-Nouby, et al. Dinov2: Learning robust visual features without supervision. *TMLR*, 2024.
- [26] William Peebles and Saining Xie. Scalable diffusion models with transformers. In *ICCV*, pages 4195–4205, 2023.
- [27] Adam Polyak, Amit Zohar, Andrew Brown, Andros Tjandra, Animesh Sinha, Ann Lee, Apoorv Vyas, Bowen Shi, Chih-Yao Ma, Ching-Yao Chuang, et al. Movie gen: A cast of media foundation models. *arXiv preprint arXiv:2410.13720*, 2024.
- [28] Robin Rombach, Andreas Blattmann, Dominik Lorenz, Patrick Esser, and Björn Ommer. High-resolution image synthesis with latent diffusion models. In *CVPR*, pages 10684–10695, 2022.
- [29] Adriana Romero, Nicolas Ballas, Samira Ebrahimi Kahou, Antoine Chassang, Carlo Gatta, and Yoshua Bengio. FitNets: Hints for thin deep nets. In *ICLR*, 2015.
- [30] Yang Song, Jascha Sohl-Dickstein, Diederik P. Kingma, Abhishek Kumar, Stefano Ermon, and Ben Poole. Score-based generative modeling through stochastic differential equations. In *ICLR*, 2021.
- [31] Hansi Teng, Hongyu Jia, Lei Sun, Lingzhi Li, Maolin Li, Mingqiu Tang, Shuai Han, Tianning Zhang, W.Q. Zhang, Weifeng Luo, et al. MAGI-1: Autoregressive video generation at scale. *arXiv preprint arXiv:2505.13211*, 2025.
- [32] Dani Valevski, Yaniv Leviathan, Moab Arar, and Shlomi Fruchter. Diffusion models are real-time game engines. In *ICLR*, 2025.
- [33] Ang Wang, Baole Ai, Bin Wen, Chaojie Mao, Chen-Wei Xie, Di Chen, Feiwu Yu, Haiming Zhao, Jianxiao Yang, Jianyuan Zeng, et al. Wan: Open and advanced large-scale video generative models. *arXiv preprint arXiv:2503.20314*, 2025.
- [34] Wenhao Wang and Yi Yang. Vidprom: A million-scale real prompt-gallery dataset for text-to-video diffusion models. In *NeurIPS*, volume 37, pages 65618–65642, 2024.

- [35] Zhuoyi Yang, Jiayan Teng, Wendi Zheng, Ming Ding, Shiyu Huang, Jiazheng Xu, Yuanming Yang, Wenyi Hong, Xiaohan Zhang, Guanyu Feng, et al. Cogvideox: Text-to-video diffusion models with an expert transformer. In *ICLR*, 2025.
- [36] Tianwei Yin, Michaël Gharbi, Taesung Park, Richard Zhang, Eli Shechtman, Frédo Durand, and William T. Freeman. Improved distribution matching distillation for fast image synthesis. In *NeurIPS*, volume 37, pages 47455–47487, 2024.
- [37] Tianwei Yin, Michaël Gharbi, Richard Zhang, Eli Shechtman, Frédo Durand, William T. Freeman, and Taesung Park. One-step diffusion with distribution matching distillation. In *CVPR*, pages 6613–6623, 2024.
- [38] Tianwei Yin, Qiang Zhang, Richard Zhang, William T. Freeman, Frédo Durand, Eli Shechtman, and Xun Huang. From slow bidirectional to fast autoregressive video diffusion models. In *CVPR*, pages 22963–22974, 2025.
- [39] Sihyun Yu, Sangkyung Kwak, Huiwon Jang, Jongheon Jeong, Jonathan Huang, Jinwoo Shin, and Saining Xie. Representation alignment for generation: Training diffusion transformers is easier than you think. In *ICLR*, 2025.
- [40] Yonghao Yu, Lang Huang, Zerun Wang, Runyi Li, and Toshihiko Yamasaki. Mirai: Autoregressive visual generation needs foresight. *arXiv preprint arXiv:2601.14671*, 2026.
- [41] Hongzhou Zhu, Min Zhao, Guande He, Hang Su, Chongxuan Li, and Jun Zhu. Causal forcing: Autoregressive diffusion distillation done right for high-quality real-time interactive video generation. *arXiv preprint arXiv:2602.02214*, 2026.

Appendix

A Implementation Details

Model architecture. The causal generator backbone is Wan2.1-T2V-1.3B [33]: 30 transformer blocks, hidden dimension 1536, FFN dim 8960, 12 heads, with QK-normalization and causal attention along the temporal axis. The foresight encoder is the frozen Wan2.1-T2V-14B: 40 blocks, hidden dimension 5120, FFN dim 13824, 40 heads, with bidirectional attention. We extract the causal generator’s hidden state at layer 15 ($\alpha = 0.5$) and the encoder’s hidden state at layer 20 ($\alpha = 0.5$, matched relative depth); the encoder is early-exited at layer 20, halving its forward cost. The predictor ϕ_ω is a stack of 3 DiT blocks [26], hidden dimension 1536, FFN ratio 4, 12 heads with QK-norm followed by a linear projection to dimension 5120. The predictor contains $\sim 138\text{M}$ parameters, accounting for $\sim 9.7\%$ of the Wan-1.3B model, and is discarded during inference.

Training pipeline. We follow the three-stage Causal-Forcing pipeline [41]: Stage 1, teacher AR fine-tuning for 2K steps; Stage 2, ODE distillation for 2K steps; Stage 3, asymmetric DMD, which is run for 100, 500, and 600 steps for chunk-wise Causal-Forcing, frame-wise Causal-Forcing, and Self-Forcing, respectively, following each baseline’s recipe. Foresight is attached only during the final 100 steps of Stage 3 in our default configuration. We also discuss applying foresight in alternative stages in Appendix D.4. At each training step, the causal generator rolls out a video, with mid-depth hidden states retained, and the foresight encoder processes the same full rollout. The foresight loss is computed on the clean rollout, while the asymmetric DMD loss is computed on a re-noised version, scored against a frozen Wan-14B real-score teacher and a Wan-1.3B fake-score critic. The fake-score critic is updated 5 times per generator update using the standard flow-matching loss, while the real-score model remains frozen throughout training.

Optimization. We use AdamW for the causal generator, predictor, and fake-score critic, with linear warmup. The causal generator and critic learning rates follow the Causal-Forcing recipe; the predictor learning rate is 2×10^{-6} . All distillation runs use $8 \times$ H100 GPUs with FSDP sharding and gradient accumulation of 8, with an effective batch size of 64. Mixed-precision training uses bf16. Training prompts come from the filtered VidProm [34] extension released by Self-Forcing.

Evaluation. We evaluate on VBench [17]. For the 5-second generation, each metric is the mean over 5 generated videos per prompt across the full VBench prompt set, following the benchmark’s standard protocol. The Total Score follows the standard VBench $0.8 \cdot \text{Quality} + 0.2 \cdot \text{Semantic}$ weighting. For the 30-second long-horizon evaluation, we roll out the same trained checkpoints on 200 randomly selected MovieGen prompts, following the Rolling-Forcing [24] protocol, and report the subset of quality and semantic dimensions that are computable under its prompt-agnostic setting, notably subject consistency, background consistency, and overall consistency, the dimensions most directly tied to causal short-sightedness.

The pseudocode for one training step is given in Algorithm 1.

B Additional Computational Cost

Video-Mirai introduces no inference-time overhead: the foresight encoder E_ϕ and predictor ϕ_ω are discarded after training, leaving the trained model as a strictly causal AR decoder with unchanged FLOPs and KV-cache behavior. Training-time overhead has two components, which we account for below by FLOP estimation on the chunk-wise Causal-Forcing pipeline at our training resolution: latent shape $1 \times 21 \times 16 \times 60 \times 104$, patch size $1 \times 2 \times 2$, giving $N_f = (60/2) \times (104/2) = 1560$ tokens per frame and $N = 21 \times N_f = 32,760$ tokens per training sample, and validate against measured wall-clock time.

Foresight encoder forward. Adding foresight to Stage 3, which is the DMD stage, requires one forward pass of encoder E_ϕ per generator update. The encoder we analyze here is the Wan-14B: $d = 5120$, FFN dim 13,824, 40 heads, 40 layers. We early-exit at layer 20 of 40, matching the student’s mid-depth layer 15 of 30, which halves the encoder’s forward cost. Each Wan-14B layer at

Algorithm 1 Video-Mirai training step

Require: causal generator G_θ , predictor ϕ_ω , frozen foresight encoder E_ϕ , fake-score critic D_ψ , frozen real-score model T , text prompt c , offset set $\Delta = \{0, \dots, K\}$, causal generator/encoder layers L, L' , weight λ

- 1: ▷ Causal generator rollout with retained mid-depth hidden states
 - 2: Initialize $\mathbf{x} \leftarrow \emptyset, \{\mathbf{h}_i^L\} \leftarrow \emptyset$
 - 3: **for** segment index $i = 1, \dots, N$ **do**
 - 4: Denoise \mathbf{X}_i conditioned on c using G_θ with KV-cache of $\mathbf{X}_{<i}$
 - 5: Cache \mathbf{h}_i^L at layer L ; append \mathbf{X}_i to \mathbf{x}
 - 6: **end for**
 - 7: ▷ Foresight encoder: one forward over the full rollout
 - 8: $\{\mathbf{H}_j^{L'}\}_{j=1}^N \leftarrow E_\phi(\mathbf{x}, c)$ at layer L' , early-exit.
 - 9: ▷ Foresight loss on valid segments
 - 10: $\bar{\mathbf{H}}_i \leftarrow \frac{1}{|\Delta|} \sum_{\delta \in \Delta} \mathbf{H}_{i+\delta}^{L'}$ for $i = 1, \dots, N-K$
 - 11: $\mathcal{L}_{\text{Foresight}} \leftarrow \frac{1}{N-K} \sum_{i=1}^{N-K} [1 - \cos(\phi_\omega(\mathbf{h}_i^L), \text{sg}[\bar{\mathbf{H}}_i])]$
 - 12: ▷ Combined objective and update
 - 13: $\mathcal{L}_{\text{Generation}} \leftarrow$ asymmetric DMD loss on re-noised rollout $\mathbf{x}_{\text{noise}}$, using frozen T and D_ψ
 - 14: $\mathcal{L}_{\text{total}} \leftarrow \mathcal{L}_{\text{Generation}} + \lambda \cdot \mathcal{L}_{\text{Foresight}}$
 - 15: Update θ and ω via $\nabla \mathcal{L}_{\text{total}}$
 - 16: ▷ Fake-score critic update (5 steps per generator step)
 - 17: Update D_ψ for 5 steps on noisy $\hat{\mathbf{x}}$ via flow-matching loss
-

$N = 32,760$ tokens contributes approximately $6Nd^2 + 4N^2d + 4Nd \cdot d_{\text{fin}} \approx 38.1$ TFLOPs forward, so 20 layers add ~ 762 TFLOPs per generator-update step. The encoder is frozen and stores no gradients, so its backward cost is zero.

Predictor forward and backward. The 3-block DiT predictor ϕ_ω runs at the causal generator’s hidden dimension $d_s = 1536$ with FFN ratio 4, FFN dim 6144 and 12 attention heads. Each block contributes ~ 8.4 TFLOPs forward, so forward across 3 blocks is ~ 25 TFLOPs and backward is ~ 51 TFLOPs ($\sim 2\times$ forward), totaling ~ 76 TFLOPs per predictor pass. A final linear projection $\mathbb{R}^{1536} \rightarrow \mathbb{R}^{5120}$ maps ϕ_ω ’s output into the encoder’s hidden width for cosine alignment; its FLOPs are negligible: ~ 1.5 TFLOPs forward+backward at $N = 32,760$, so the predictor pass remains ~ 76 TFLOPs.

Parameter and optimizer-state overhead. The predictor ϕ_ω contains $\sim 138\text{M}$ trainable parameters in total: $\sim 130\text{M}$ from the 3 DiT blocks plus $\sim 7.9\text{M}$ from the final $1536 \rightarrow 5120$ linear projection, which is $\sim 9.7\%$ of the Wan-1.3B causal generator. Under AdamW with FSDP sharding across our 8 training GPUs, the per-GPU optimizer-state increase is approximately $207\text{MB} \approx 138\text{M} \times 12 \text{ bytes/param} / 8$.

Per-cycle FLOP accounting. A standard asymmetric DMD training cycle consists of 1 generator update step and 5 critic update steps. Without foresight:

- **Generator update.** 4398 TFLOPs $\approx 3 \times 270$ TFLOPs (Wan-1.3B, causal generator, forward and backward) + 2×1524 TFLOPs (Wan-14B, real-score teacher, conditional and unconditional forward) + 2×270 TFLOPs (Wan-1.3B, fake-score critic, conditional and unconditional forward)
- **Critic update** ($\times 5$). 810 TFLOPs $\approx 3 \times 270$ TFLOPs (Wan-1.3B, fake-score critic, forward and backward).

With foresight enabled, the generator-update step adds 838 TFLOPs (762 from E_ϕ and 76 from ϕ_ω). We additionally update ϕ_ω during each critic step using cached hidden states, adding 76 TFLOPs per critic step. This replay amortizes the encoder cost across the DMD cycle: E_ϕ runs only on the generator step, while the predictor benefits from more frequent updates. The total per-cycle cost is 8448 TFLOPs without foresight and 9666 TFLOPs with foresight, a relative overhead of approximately **14%**.

Empirical wall-clock measurement. We validate this estimate by measuring per-step training time on $8 \times$ H100 GPUs over approximately 100 training steps with foresight enabled and disabled, under otherwise identical Stage 3 configuration. The asymmetric DMD schedule produces a 1-in-5 cyclic pattern: one generator update followed by five critic updates, so we report the two-step types separately in Table 7. The measured per-cycle overhead of **13.7%** closely matches the FLOP-based estimate.

Table 7: **Empirical wall-clock training time per step.** Measured on $8 \times$ H100 over 100 training steps each. Per-cycle overhead 13.7% matches the FLOP-based estimate closely.

Step type	Baseline (s)	+ Foresight (s)	Overhead
Generator update	244	292	+20.0%
Critic update	86	95	+10.6%
Per-cycle (1 gen + 5 critic)	674	767	+ 13.7%

Inference cost. At deployment, the student runs without E_ϕ , ϕ_ω , or the foresight loss. The inference cost is identical to a standard causal Wan-1.3B forward pass, and the KV cache is maintained as in any causal AR generator. Real-time streaming properties like the latency per frame or throughput are also unchanged from the Causal-Forcing baseline.

C Limitations

Our foresight window is deliberately small: the default $\Delta = \{0, 1\}$ looks at most one chunk ahead, roughly 3 latent frames (~ 0.75 seconds at 16 fps). Our ablations show that naively extending the window further within the current recipe yields diminishing returns (Table 1): adding a two-step-ahead target ($\Delta = \{0, 1, 2\}$) improves Semantic but degrades Quality, and the number of valid (source, target) pairs shrinks as K grows since supervising chunk i requires access to chunk $i + K$. Given how clearly anticipation is internalized at short horizons (Figure 5), an open question is whether a longer training-time foresight window could deliver proportional gains at longer generation horizons. Promising directions include longer rollouts with position-reweighted foresight loss, hierarchical alignment at multiple timescales, and virtual chunks that extrapolate beyond the rollout horizon. We leave these to future work.

D Additional Results

D.1 Full VBench

Tables 8 and 9 report the detailed per-dimension breakdown of VBench Quality and Semantic Scores, covering 7 and 9 dimensions respectively, for the Causal-Forcing baseline and after applying Video-Mirai. We evaluate both 5-second generation under the VBench standard protocol and 30-second long-horizon generation using MovieGen prompts under the VBench prompt-agnostic protocol.

Table 8: **Per-dimension Quality Score on VBench.**

Method	Subject Consistency	Background Consistency	Temporal Flickering	Motion Smoothness	Dynamic Degree	Aesthetic Quality	Imaging Quality	Quality Score
<i>5-second</i>								
Causal-Forcing	96.05	95.92	98.64	98.26	61.11	67.01	70.92	84.54
+ Video-Mirai	96.41	96.54	99.42	98.33	65.00	67.88	69.87	85.38
<i>30-second</i>								
Causal-Forcing	84.93	90.22	96.04	97.21	49.00	56.90	64.54	76.26
+ Video-Mirai	88.47	91.94	95.93	97.16	49.50	61.52	64.25	77.88

Table 9: **Per-dimension Semantic Score on VBench.**

Method	Object Class	Multiple Objects	Human Action	Color	Spatial Relation	Scene	Temporal Style	Appearance Style	Overall Consistency	Semantic Score
<i>5-second</i>										
Causal-Forcing	95.98	88.66	95.60	86.89	78.40	57.05	24.62	20.63	26.83	80.93
+ Video-Mirai	96.79	87.96	95.40	87.26	82.29	57.57	24.83	20.76	26.85	81.59
<i>30-second</i>										
Causal-Forcing	–	–	–	–	–	–	24.93	–	24.93	–
+ Video-Mirai	–	–	–	–	–	–	25.03	–	25.03	–

Table 10: **Frame-wise foresight window comparison.** Effect of the offset set Δ on top of the Causal-Forcing frame-wise.

Setting	Δ	Quality \uparrow	Semantic \uparrow	Total \uparrow
Causal-Forcing (frame-wise)	–	83.16	78.73	82.27
Current only	{0}	83.81	79.50	82.94
1-frame ahead only	{1}	83.79	79.66	82.96
Current + 1-frame ahead	{0, 1}	84.21	79.41	83.25
Current + 2-frame ahead	{0, 1, 2}	83.25	77.80	82.16

D.2 Framewise Foresight Window

Table 10 extends our foresight window study (Table 1) to the frame-wise setting, where each segment is a single latent frame. The chunk-wise conclusion holds: $\Delta=\{0, 1\}$ achieves the best Total Score, extending to $\{0, 1, 2\}$ drops the Total Score, below the baseline, showing that the encoder’s features at far future offsets become too noisy to provide a useful learning signal.

D.3 Loss Weight

Table 11 sweeps the foresight weight $\lambda \in \{0.1, 0.2, 0.3\}$ on Causal-Forcing. $\lambda=0.2$ achieves the best Total Score: lower weights under-supervise the predictor and yield smaller gains, while higher weights over-pull the causal generator’s mid-depth features toward the encoder and slightly degrade the Quality Score. We adopt $\lambda=0.2$ throughout.

Table 11: **Foresight weight λ ablation** on Causal-Forcing.

Weight	Quality \uparrow	Semantic \uparrow	Total \uparrow
Causal-Forcing	84.54	80.93	83.82
0.1	84.83	81.42	84.15
0.2	85.38	81.59	84.62
0.3	85.14	81.71	84.45

D.4 Foresight at Different Distillation Stages

Causal-Forcing exposes two training stages at which Video-Mirai can be attached: Stage 2, causal ODE distillation, and Stage 3, asymmetric DMD. These two stages are not interchangeable injection points because they differ in what data the causal generator consumes. In this section, we analyze how to inject foresight into Stage 2.

Stage 2 ODE: target from the ground-truth future. Stage 2 trains the causal generator’s flow map on paired (noise \rightarrow clean) trajectories whose clean side is a ground-truth video $\{\mathbf{X}_1^{\text{GT}}, \dots, \mathbf{X}_N^{\text{GT}}\}$. The causal generator is teacher-forced on clean GT prefixes, and the ODE distillation loss is defined on GT trajectories. The consistent foresight target is therefore the GT future segment: at each step,

we feed the clean latent of $\mathbf{X}_{i+\delta}^{\text{GT}}$ to the foresight encoder. Both the ODE loss and the foresight loss live on the same clean, teacher-forced manifold.

Stage 3 DMD: target from the causal generator’s own rollout. Stage 3 removes the paired data: the causal generator self-rolls a video $\{\mathbf{X}_1, \dots, \mathbf{X}_N\}$ from noise, and asymmetric DMD matches the causal generator’s output distribution to a bidirectional teacher’s score. The consistent foresight target is the foresight encoder’s representation of the causal generator’s own future rollout. Foresight then regularizes the same trajectory and distribution that DMD already matches, ensuring the two objectives operate on a shared signal.

Ablation study of foresight in Stage 2. The main paper studies foresight at Stage 3 (DMD). For completeness, we conduct two parallel ablations within Stage 2 (ODE) along the same axes as the main paper’s Stage 3 counterparts: the foresight encoder and the predictor’s fusion strategy. All Stage 2 runs use 1K distillation steps and no Stage 3 refinement.

Table 12 fixes the encoder to Wan-14B and sweeps three fusion strategies for the offset set $\Delta=\{0, 1\}$: no fusion (one loss per offset), per-frame averaging (encoder features averaged across frames within each segment), and per- δ averaging (encoder features averaged across offsets, i.e., the default in the main paper, Eq. 4). Table 13 fixes the fusion strategy to per-frame averaging and sweeps the encoder among EMA, Wan-1.3B, and Wan-14B. Two findings emerge. First, at Stage 2, per- δ averaging is actively harmful, while per-frame averaging is best. This contrasts with Stage 3, where per- δ target fusion is optimal. The two stages train on different data: ODE pairs of GT videos versus the causal generator’s own rollouts. The fusion strategy that aligns with each stage’s data is what wins. Second, Wan-14B remains the strongest encoder at Stage 2, mirroring the Stage 3 ordering in Table 4.

Table 12: **Stage 2 fusion-strategy ablation.** Encoder fixed to Wan-14B with 1K steps training.

Fusion strategy	Quality \uparrow	Semantic \uparrow	Total \uparrow
Causal-Forcing (stage 2 reproduction)	82.56	78.30	81.71
no fusion	82.65	77.51	81.62
per-frame averaging	84.17	77.68	82.87
per- δ averaging	81.45	74.32	80.02

Table 13: **Stage 2 encoder ablation.** Fusion strategy fixed to per-frame averaging with 1K steps training.

Encoder	Quality \uparrow	Semantic \uparrow	Total \uparrow
Causal-Forcing (stage 2 reproduction)	82.56	78.30	81.71
EMA	83.96	78.01	82.77
Wan-1.3B	83.40	78.76	82.47
Wan-14B	84.17	77.68	82.87

Foresight injection stage comparison. Causal-Forcing’s three-stage pipeline exposes two natural injection points for foresight: ODE distillation (Stage 2) and asymmetric DMD (Stage 3). Whether to attach foresight at Stage 2, Stage 3, or both is not *a priori* obvious. Table 14 sweeps all three options. The results show that ODE-Foresight and DMD-Foresight yield identical total gains over Causal-Forcing, but split the credit very differently: ODE-Foresight drives the largest quality gain while leaving semantic drop, consistent with pulling the flow map toward a clean, well-formed future, whereas DMD-Foresight drives the largest semantic gain while retaining most of the quality improvement, consistent with regularizing the very distribution DMD is already matching, on the same rollout trajectory.

Stacking the two does not combine these profiles, collapsing to a Total Score only marginally above the baseline. The reason is that the two instantiations do not disagree about *whether* the causal generator should anticipate the future, but about *which* future: ODE-Foresight trains ϕ_ω to predict a clean GT future from a GT prefix, while DMD-Foresight trains it to predict the future from the causal

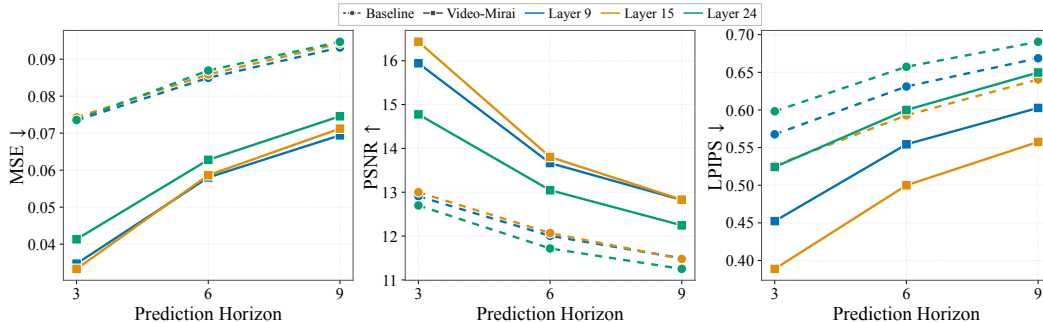


Figure 8: **Future-frame readout fidelity across layers and horizons.** Solid: Video-Mirai; dashed: Causal-Forcing baseline. Video-Mirai dominates at every layer and horizon.

generator’s *own* rollout, and the two trajectories differ whenever the causal generator is imperfect. Stacked naively, Stage 3 must rewrite the foresight mapping Stage 2 just installed, swapping a clean target for a moving one while simultaneously running asymmetric DMD; these pressures pull mid-depth features in conflicting directions.

DMD-Foresight is the most practical choice since it is the most effective and cheapest: it drops into any pretrained Causal-Forcing Stage 2 checkpoint without modifying Stage 2 training, and requires only 100 DMD steps, $20\times$ fewer than the 2K Stage 2 distillation steps. We therefore use it throughout the main paper.

Table 14: **Foresight injection stage comparison.** Foresight applied at Stage 2 (ODE-Foresight), Stage 3 (DMD-Foresight), or both.

Stage	Quality ↑	Semantic ↑	Total ↑
Causal-Forcing	84.54	80.93	83.82
Stage 2	85.56	80.84	84.62
Stage 3	85.38	81.59	84.62
Stage 2 + 3	84.78	81.10	84.05

E Statistical Significance

We test whether Video-Mirai’s gains over Causal-Forcing chunk-wise are statistically significant via a paired prompt-level bootstrap. For each VBench dimension, we resample its N_d prompts with replacement, using the same indices for both methods and recompute the dimension’s mean, repeating 10,000 times. Each replicate is then aggregated into Quality, Semantic, and total Scores using VBench’s standard $\frac{4}{5}$ quality + $\frac{1}{5}$ semantic weighting [17], yielding bootstrap distributions of the three summary metrics. We report standard errors and [2.5%, 97.5%] percentile 95% CIs of the paired difference; a * marks CIs that exclude zero (two-sided $p < 0.05$). Per-prompt scores are obtained by averaging the 5 inference seeds per prompt. We do not retrain Video-Mirai with multiple random seeds due to the substantial GPU cost of each Stage 3 distillation run, which is consistent with prior work in video distillation [16, 41].

Table 15 shows that Video-Mirai’s gains on all three aggregated metrics have 95% CIs strictly excluding zero, confirming the improvements are not driven by a small subset of favorable prompts.

Table 15: **Significance of Video-Mirai gains over Causal-Forcing on VBench.** 10,000 paired bootstrap resamples by prompt; cells: $\Delta_{\text{mean}} \pm \text{SE}$. * marks 95% confidence intervals excluding zero, equivalent to a two-sided $p < 0.05$ test.

Method	Δ Quality	Δ Semantic	Δ Total
Video-Mirai (vs Causal-Forcing)	$+0.84 \pm 0.19^*$	$+0.66 \pm 0.24^*$	$+0.80 \pm 0.15^*$

F More Probing Results

We provide additional visualization results of our probing analysis in Figures 8 and 9.

G More Comparison Results

We provide additional visual comparisons in Figure 10.



Figure 9: **Video-Mirai’s representations encode the future.** An MLP readout reconstructs future RGB from the frozen causal generator’s current hidden state (layer 15). Left to right: current frame, baseline readout, Video-Mirai readout (ours), future frame. **blue/red**: regions matching the **current/future** frame.

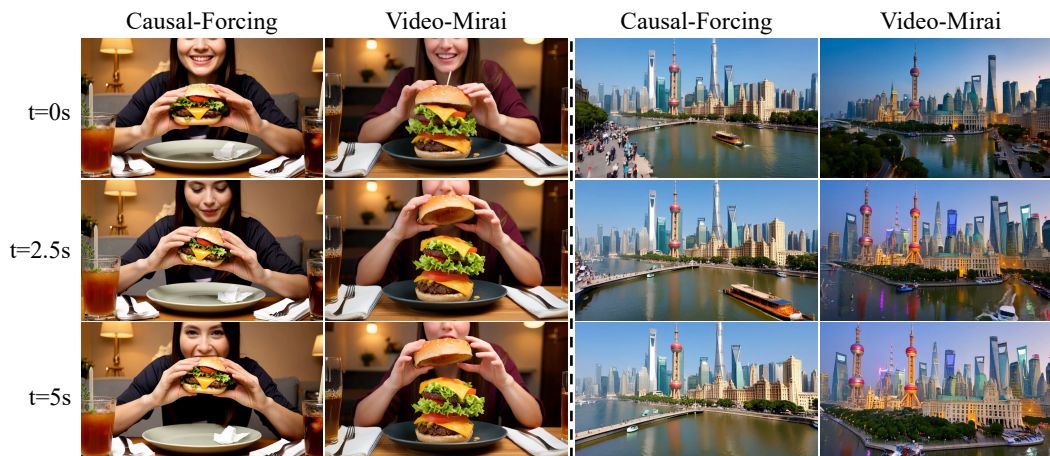


Figure 10: **More qualitative comparison.** Representative frames at $t=0s$, $2.5s$, $5s$ from the rollouts of the same prompt under the baseline and Video-Mirai counterpart. Video-Mirai rollouts preserve subject identity, scene composition, and motion coherence more reliably across time.